Optimal "image-based" weighting for energy-resolved CT

Taly Gilat Schmidt[a)]
Department of Biomedical Engineering, Marquette University, Milwaukee, Wisconsin 53201

This paper investigates a method of reconstructing images from energy-resolved CT data with negligible beam-hardening artifacts and improved contrast-to-nosie ratio (CNR) compared to conventional energy-weighting methods. Conceptually, the investigated method first reconstructs separate images from each energy bin. The final image is a linear combination of the energy-bin images, with the weights chosen to maximize the CNR in the final image. The optimal weight of a particular energy-bin image is derived to be proportional to the contrast-to-noise-variance ratio in that image. The investigated weighting method is referred to as "image-based" weighting, although, as will be described, the weights can be calculated and the energy-bin data combined prior to reconstruction. The performance of optimal image-based energy weighting with respect to CNR and beam-hardening artifacts was investigated through simulations and compared to that of energy integrating, photon counting, and previously studied optimal "projection-based" energy weighting. Two acquisitions were simulated: dedicated breast CT and a conventional thorax scan. The energy-resolving detector was simulated with five energy bins. Four methods of estimating the optimal weights were investigated, including task-specific and task-independent methods and methods that require a single reconstruction versus multiple reconstructions. Results demonstrated that optimal image-based weighting improved the CNR compared to energy-integrating weighting by factors of 1.15–1.6 depending on the task. Compared to photon-counting weighting, the CNR improvement ranged from 1.0 to 1.3. The CNR improvement factors were comparable to those of projection-based optimal energy weighting. The beam-hardening cupping artifact increased from 5.2% for energy-integrating weighting to 12.8% for optimal projection-based weighting, while optimal image-based weighting reduced the cupping to 0.6%. Overall, optimal image-based energy weighting provides images with negligible beam-hardening artifacts and improved CNR compared to energy-integrating and photon-counting methods. © *2009 American Association of Physicists in Medicine.* [DOI: 10.1118/1.3148535]

Key words: computed tomography, energy weighting, photon counting, beam-hardening artifacts

I. INTRODUCTION

Recent advances in detector technology have enabled computed tomography (CT) systems with energy resolving capabilities. X-ray attenuation depends on photon energy, and this energy dependence varies for different materials. Therefore, the energy of a detected photon is an additional piece of information that may be used to improve image reconstruction. Properly accounting for the incident polyenergetic spectrum has the additional benefit of eliminating beam-hardening artifacts.

An energy-resolving detector with two energy bins (low and high energies) enables simultaneous dual-energy acquisition for material decomposition applications.[1–3] Once decomposed, monoenergetic images free of beam-hardening artifacts are possible.[4] Depending on the chosen energy, the monoenergetic images may be reconstructed without noise penalty.[4] An energy-resolving detector with three energy bins enables *K*-edge imaging to improve the depiction of contrast agents such as gadolinium.[5,6]

An energy-resolving detector with multiple energy bins provides improved utilization of spectral information.[7] Conventional energy-integrating detectors weight each photon by its energy, thereby assigning more weight to higher energy photons. A photon-counting detector assigns equal weight to all photons. These weighting schemes are suboptimal because the contrast between materials is generally greater at low energies. Ideally, a detector would give more weight to the low-energy photons. An optimal energy-weighting scheme was developed to maximize the contrast-to-noise ratio (CNR) in x-ray projections.[7] The optimal weighting scheme weights all photons at a particular energy *E* proportionally to the signal and inversely proportional to the noise variance of the projection data at energy *E*.

Previous work has applied these optimal weights to simulated and experimental energy-resolved CT data.[2,3,8–10] In these studies, energy-bin data were optimally weighted and combined prior to log normalization and reconstruction. This energy-weighting approach is referred to as optimal "projection-based" energy weighting. Photon counting and energy integrating are examples of suboptimal projection-based weighting. Previous simulation and experimental studies demonstrated a 1.2–1.6 improvement in CNR for breast CT imaging using optimal projection-based weighting.[2,3] By giving more weight to low energy photons, projection-based weighting increases both the CNR and beam-hardening artifacts in the reconstructed image.[2,9]

Gleason *et al.*, developed a small-animal CT system with an energy-resolving detector and performed separate reconstructions on the data in each energy bin.[11] The authors suggest a linear combination of the resulting energy-bin images but did not recommend a specific weighting scheme. An optimal "image-based" linear combination was first proposed by Niederlohner *et al.*, in which the weights were calculated numerically using the Downhill–Simplex method.[12,13] While the details of the iterative algorithm are limited, the work demonstrated CNR comparable to optimal projection-based weighting with a qualitative reduction in beam-hardening artifacts.

This paper further investigates the image-based energy-weighting method that optimally weights and combines the energy-bin images. Unlike the previously proposed iterative algorithm, the weights proposed in the current study are calculated analytically to maximize the CNR in the combined image. For each energy-bin image, the optimal weight is proportional to the contrast-to-noise-variance ratio (CNVR) in the image. Because the energy-bin images are reconstructed from data acquired by a narrow polyenergetic spectrum, and because the energy-bin data are weighted and combined after log normalization, beam-hardening artifacts are reduced compared to conventional approaches. As will be described, although the weights are conceptually derived from the reconstructed energy-bin images, the weights can be calculated prior to reconstruction and the data combined after log normalization.

This paper first reviews the theory of the optimal projection-based weights and then describes the theoretical derivation and implementation of the optimal image-based weights. Simulations are presented that compare the optimal projection and image-based weighting schemes with respect to CNR and beam-hardening artifacts for a breast and thorax application. The CNR and beam-hardening effects are also compared to images reconstructed from energy-integrating and photon-counting detectors.

II. METHODS AND MATERIALS

II.A. Theoretical considerations

II.A.1. Projection-based optimal energy weighting

The line integral ℓ estimated by a conventional polyenergetic CT acquisition is described in Eq. (1), where $N_o(E)$ is the number of incident photons at each energy E, $w(E)$ is the energy-dependent weight, and $\mu(l,E)$ is the energy-dependant linear attenuation coefficient of the object along ray path l,

$$\ell = -\ln\left(\frac{\int w(E) \cdot N_o(E) e^{-\int \mu(l,E)dl} dE}{\int w(E) \cdot N_o(E) dE}\right). \tag{1}$$

For example, $w(E)=E$ for energy-integrating detectors and $w(E)=1$ for photon-counting detectors. Previous work proposed optimal weights for maximizing the CNR between a projection through background material and a projection through background material with an embedded contrast element of length d.[2,7] The optimal weights are proportional to

the CNVR of the projection data and are expressed in Eq. (2), where μ_b and μ_c are the linear attenuation coefficients of the background and contrast element materials, respectively. As is evident in Eq. (2), the optimal weights depend on the specific task,

$$w(E) = \frac{1 - e^{-[\mu_c(E) - \mu_b(E)]d}}{1 + e^{-[\mu_c(E) - \mu_b(E)]d}}. \tag{2}$$

In practice, energy-resolving detectors separate the incoming photons into discrete energy bins. Previous studies have applied the optimal projection-based weights of Eq. (2) to detectors with discrete energy bins.[2,3,8–10] The estimated line integral $\widetilde{\ell}_{pb}$ is described in Eq. (3), where M is the number of energy bins and E_i is the energy range of the ith bin,

$$\widetilde{\ell}_{pb} = -\ln\left(\frac{\sum_{i=1}^{M}(w_i \cdot \int_{E_i} N_o(E) e^{-\int \mu(l,E)dl} dE)}{\sum_{i=1}^{M} w_i \cdot \int_{E_i} N_o(E) dE}\right). \tag{3}$$

The weighting scheme described in Eq. (3) performs a linear combination of the energy-bin data prior to log normalization and reconstruction. Another approach for projection-based weighting is to weight and combine the energy-bin data after raw-beam normalization but before the logarithm. This approach requires modified optimal weights that are derived in the appendix. The results in the appendix demonstrate that both forms of projection-based weighting result in similar CNR and beam-hardening performance. Therefore, the remainder of the paper considers the projection-based weighting described in Eq. (3).

II.A.2. Image-based optimal energy weighting

This paper investigates an optimal linear combination of the reconstructed energy-bin images. The combined image is expressed in Eq. (4) where M is the number of energy bins and w_i is the weight of the ith energy-bin image,

$$\text{Image}_{\text{combined}} = \sum_{i=1}^{M} w_i \cdot \text{Image}_i. \tag{4}$$

In this discussion, the contrast is defined as the absolute difference between the reconstructed attenuation coefficients of two materials. The contrast in the ith energy-bin image, C_i, is defined in Eq. (5), where $\mu_{c,i}$ and $\mu_{b,i}$ are the reconstructed attenuation coefficients of the contrast element and background material in the ith energy-bin image. The contrast depends on the energy range of the bin,

$$C_i = |\mu_{c,i} - \mu_{b,i}|. \tag{5}$$

The noise is defined as the standard deviation in a background region of the image. The noise standard deviation in the ith energy-bin image, σ_i, depends on number of photons detected in the bin and the spatial resolution. When an image is weighted, both the signal and standard deviation of the image are multiplied by the weight. When the images are combined, the signals add and the variances add. The CNR of the combined image is

$$\text{CNR}_{\text{combined}} = \frac{\sum_{i=1}^{M} w_i \cdot C_i}{(\sum_{i=1}^{M} w_i^2 \cdot \sigma_i^2)^{1/2}}. \tag{6}$$

This paper considers how to combine the M energy-bin images in order to maximize the CNR of the final image. In the absence of noise, all of the weight would be given to the energy bin with the highest contrast (generally the low energy bin). In practice, the data from the lowest energy bin are generally noisiest because of the small number of detected photons.

The derivative of the CNR of the combined image with respect to the weight of the nth energy bin w_n is

$$\frac{\partial \text{CNR}_{\text{combined}}}{\partial w_n} = \frac{C_n \cdot \sum_{i=1}^{M} w_i^2 \sigma_i^2 - w_n \sigma_n^2 \cdot \sum_{i=1}^{M} w_i C_i}{(\sum_{i=1}^{M} w_i^2 \cdot \sigma_i^2)^{3/2}}. \tag{7}$$

A solution to this optimization problem is to weight each image proportionally to CNVR. For example, the weight of the nth energy-bin image is

$$w_n \propto \frac{C_n}{\sigma_n^2}. \tag{8}$$

When the weights of Eq. (8) are substituted into Eq. (7), the resulting expression is

$$\frac{\partial \text{CNR}_{\text{combined}}}{\partial w_n} = \frac{(C_n - C_n) \cdot \sum_{i=1}^{M} (C_i/\sigma_i)^2}{(\sum_{i=1}^{M} (C_i/\sigma_i)^2)^{3/2}} = 0. \tag{9}$$

Equation (9) proves that weighting each image proportionally to the CNVR maximizes the CNR of the combined image. The M weights are further constrained to have a sum of one, as expressed in Eq. (10). As in the case of the projection-based weighting, the optimal weights are task dependent,

$$w_n = \frac{C_n/\sigma_n^2}{\sum_{i=1}^{M} C_i/\sigma_i^2}. \tag{10}$$

Assuming that the weights can be estimated prior to reconstruction (as will be described in Sec. II B 3) and assuming a linear reconstruction algorithm such as filtered backprojection, an equivalent result is obtained by weighting and combining the energy-bin data after log normalization but before reconstruction. In this case only one reconstruction of the combined energy-bin data is required. In comparison to the line integral estimated by projection-based weighting [Eq. (3)], the estimated line integral after image-based weighting $\tilde{\ell}_{ib}$ is

$$\tilde{\ell}_{ib} = \sum_{i=1}^{M} - w_i \ln \left(\frac{\int_{E_i} N_o(E) e^{-\int \mu(l,E)dl} dE}{\int_{E_i} N_o(E) dE} \right). \tag{11}$$

II.A.3. Beam-hardening artifacts

In the case of monoenergetic x rays, the number of photons that pass through an object of thickness t and attenuation coefficient μ is described by the Beer–Lambert law,

$$N = N_o \cdot e^{-\mu \cdot t}. \tag{12}$$

The logarithm of the transmission varies linearly with material thickness,

$$\ln \left(\frac{N}{N_o} \right) = - \mu \cdot t. \tag{13}$$

When polyenergetic data are acquired with conventional energy-weighting schemes, the logarithm of the transmission has a nonlinear dependence on thickness. Beam-hardening artifacts occur because the reconstructed attenuation coefficient depends on the material thickness.[14]

Equations (3) and (11) express the line integrals estimated by the projection and image-based energy-weighting schemes. If the object is a homogenous slab of thickness t and attenuation μ, and each of the M energy bins detects monoenergetic photons, the line integrals estimated by projection and image-based weighting are given in Eqs. (14) and (15),

$$\tilde{\ell}_{pb} = - \ln \left(\frac{\sum_{i=1}^{M} w_i \cdot N_o(E_i) e^{-\mu(E_i)t}}{\sum_{i=1}^{M} w_i \cdot N_o(E_i)} \right), \tag{14}$$

$$\tilde{\ell}_{ib} = \sum_{i=1}^{M} - w_i \ln \left(\frac{N_o(E_i) e^{-\mu(E_i)t}}{N_o(E_i)} \right) = \sum_{i=1}^{M} w_i \cdot \mu(E_i) \cdot t. \tag{15}$$

The line integral estimated by image-based weighting is linear with material thickness, while the projection-based estimate has a nonlinear dependence on material thickness.

If the material thickness is known, the attenuation coefficient can be determined by dividing the estimated line integral by the thickness. The attenuation coefficients estimated by projection-based weighting and image-based weighting are expressed in Eqs. (16) and (17),

$$\tilde{\mu}_{pb} = - \ln \left(\frac{\sum_{i=1}^{M} w_i \cdot N_o(E_i) e^{-\mu(E_i)t}}{\sum_{i=1}^{M} w_i \cdot N_o(E_i)} \right) \cdot \frac{1}{t}, \tag{16}$$

$$\tilde{\mu}_{ib} = \sum_{i=1}^{M} w_i \cdot \mu(E_i). \tag{17}$$

The projection-based estimate of μ depends on material thickness, while the image-based estimate is independent of thickness, thereby preventing beam-hardening artifacts. For all slab thicknesses, the image-based estimate of μ is the weighted average of attenuation coefficients across energy.

The beam-hardening analysis in Eqs. (14)–(17) assumed ideal monoenergetic x rays. The general image-based weighting described in Eq. (11) is expected to reduce beam-hardening artifacts because the log normalization occurs over a narrow range of energies, thereby approximating the monoenergetic case.

II.B. Simulation study

The purpose of the simulation study was to test the feasibility of optimal image-based energy weighting and to compare the performance to that of projection-based weighting (optimal, photon counting, and energy integrating) with respect to CNR and beam-hardening artifacts.

TABLE I. Simulated fan-beam system specifications.

	Breast	Thorax
Number of detectors	2048	2048
Pixel size	0.4 mm	0.4 mm
Source-to-isocenter distance (SID)	60 cm	54 cm
Source-to-detector distance (SDD)	80 cm	95 cm
Number of views	500	500
Spectrum	90 kVp, 2 mm Al	120 kVp, 6 mm Al
Raw incident photons per detector per view	32 400	150 000
mAs	39	250

II.B.1. Systems and phantoms

The image-based energy-weighting method was applied to two CT applications: a thorax scan and a dedicated breast CT acquisition. The simulation details are listed in Table I. The breast CT phantom and simulation are similar to that of a published optimal projection-based weighting study.[2] All studies simulated a 2D fan-beam geometry. The spectra were modeled with an published technique.[15] The chosen mAs levels represent a breast CT scan with dose equivalent to mammography and a typical thorax examination.[16] The mAs values were converted to the number of incident photons per detector using typical photon fluence values for breast and conventional CT acquisitions.[16,17]

The breast phantom consisted of a 14-cm-diameter disk with the attenuation properties of 50% adipose/50% glandular tissue. The breast phantom contained three, 2-cm-diameter contrast elements of adipose tissue, 0.28 g/cm^3 CaCO$_3$, and 2.5 mg/cm^3 iodine. The contrast elements were centered 4 cm from the phantom center. The thorax phantom was based on the FORBILD thorax phantom with the addition of a 2-cm-diameter region of 7.5 mg/cm^3 iodine located in the heart and with the ribs and vertebrae removed to accommodate the available CT simulation software.[18] Material compositions were based on ICRU Report No. 44 and the attenuation coefficients were modeled with the NIST online database.[19,20]

Monoenergetic fan-beam projections were calculated analytically at 20–90 keV in 0.5 keV increments for the breast scan and at 20–120 keV in 0.5 keV increments for the thorax scan. Poisson noise was added to each monoenergetic projection with variance equal to the number of detected photons at that energy. Only noise due to photon statistics was modeled, as photon-counting detectors are expected to have negligible electronic and detector noise.[21]

II.B.2. Energy-resolving detector

The simulated detector was ideal in that it detected all incident photons, performed perfect energy resolution, and was unlimited in count rate.

The effect of the number of energy bins on CNR was previously studied for optimal projection-based energy weighting.[2] The results demonstrated that increasing the number of bins from 5 to 15 did not considerably improve the CNR. Following the example of previous studies, five energy bins were simulated with narrower bin widths at low energies to better sample the spectrum. Table II lists the energy ranges of the simulated bins for the 90 and 120 kVp spectra. For the thorax acquisition, the width of the lowest energy bin was chosen to include the k-edge in order to reduce the effects of photon starvation, otherwise no attempt was made to optimize the bin widths. The average energy of each of the i bins, $\bar{E}_i$, which is used to calculate the optimal weights, was estimated as the mean energy of the unattenuated spectrum detected by the bin [Eq. (18)],

$$\bar{E}_i = \frac{\int_{E_i} E \cdot N_o(E)dE}{\int_{E_i} N_o(E)dE}.$$ (18)

Energy bins that did not detect photons (i.e., photon starved) were set to 0.5 prior to log normalization. To quantify the magnitude of photon starvation, the percentage of photon-starved pixels in each energy bin was calculated.

II.B.3. Optimal image-based weights

The optimal image-based weights, proportional to the CNVR, must characterize the energy dependence of the contrast and noise variance in the images. Numerous methods are available for estimating contrast and noise in a recon-

TABLE II. Simulated detector energy bins.

Bin number		1	2	3	4	5
Breast (90 kVp spectrum)	Range (keV)	20–28	28–36	36–48	48–58	58–90
	Average (keV)	25.3	32.5	42.2	53.2	67.5
Thorax (120 kVp spectrum)	Range (keV)	20–35	35–45	45–60	60–90	90–120
	Average (keV)	31.0	40.1	53.1	70.8	99.8

TABLE III. Investigated weight-calculation methods.

Method	Contrast estimate	Noise variance estimate	Task specific	Multiple reconstructions
A	μ look-up table	Image based (ROI)	Yes	Yes
B	μ look-up table	Projection based [Eq. (20)]	Yes	No
C	$1/E^3$	Image based (ROI)	No	Yes
D	$1/E^3$	Projection based [Eq. (20)]	No	No

structed CT image, and two methods for estimating the contrast and two methods for estimating the noise variance were investigated.

Recall that in this work, the contrast is defined as the difference in the linear attenuation coefficient of two materials. The contrast of a specific task can be measured through regions of interest (ROIs) in the reconstructed energy-bin images, however, suitable regions may be difficult to locate in clinical images. Therefore, two alternative methods for estimating contrast were investigated. The contrast of a specific task in a particular energy-bin image can be calculated in advance from known linear attenuation coefficients and stored in a lookup table. The average attenuation coefficient of a material in the ith energy bin, $\bar{\mu}_i$, is expressed in Eq. (19), where $\mu(E)$ is available in the literature, for example, from Ref. 20,

$$\bar{\mu}_i = \frac{\int_{E_i} \mu(E) \cdot N_o(E) dE}{\int_{E_i} N_o(E) dE}. \tag{19}$$

Calculating the weights based on look-up tables requires prior knowledge of the imaging task to be optimized. A reconstruction may be desired that, while not optimal for specific tasks, provides a general improvement in image quality. Previous work approximated the energy dependence of the contrast as $1/E^3$, where E is the average bin energy [Eq. (18)].[10] This function accounts for the energy dependence of the photoelectric effect and is most accurate at low energies and for materials with high atomic number. Another limitation of this weighting function is that it does not characterize the K-edge effect. While limited in accuracy, this approximation may be useful as a general method for calculating the image-based weights.

The noise variance in the reconstructed image can be measured in a ROI or it can be calculated from the projection data. The noise variance of a reconstructed CT voxel is proportional to the number of photons that pass through the voxel and are detected as expressed in Eq. (20), where σ_i^2 is the variance of a voxel in the ith energy-bin image, m is the number of views, and N_{ij} is the number of detected photons in the ith energy bin of the detector that samples the voxel in the jth view,[22]

$$\sigma_i^2 \propto \sum_{j=1}^{m} \frac{1}{N_{ij}}. \tag{20}$$

In this study, N_{ij} was calculated for the ith energy bin as the mean number of detected photons in the central 100 detectors of the jth view. For the ROI based noise estimate, the standard deviation was calculated in a 25×25 pixel ROI extracted from the background breast and heart regions for the breast and thorax simulations, respectively. A limitation of both of these methods is that they characterize the noise variance in a region of the image. However, the weights must reflect the energy dependence of the noise variance, which is expected to be fairly constant throughout the image. Table III summarizes the investigated weight-calculation methods. Methods A and B, which rely on look-up tables of attenuation coefficients, are task specific, while methods C and D are independent of task. Since the breast phantom contained three imaging tasks, methods A and B were repeated three times with weights optimized for each of the three contrast elements. Methods B and D estimate the noise variance from the projection data and can be applied prior to reconstruction, while methods A and C require reconstruction from each energy bin. For the simulations described in this work, all four methods were implemented by weighting and combining the energy-bin data after reconstruction.

II.B.4. Projection-based weights

For comparison, images were reconstructed assuming ideal photon-counting and energy-integrating detectors. In these cases, the simulated monoenergetic projections were weighted by E (energy integrating) and 1 (photon counting) and combined prior to log normalization.

The energy-resolved data were also reconstructed with optimal projection-based weighting. Because the optimal projection-based weights are task dependent, three reconstructions were performed for the breast phantom with weights optimized for each of the three contrast elements. For the thorax phantom, the optimal weights were calculated to maximize the CNR between 0.75 mg/cm³ iodine and water. The optimal projection-based weights were calculated with Eq. (2) assuming the average attenuation coefficients of Eq. (19).

II.B.5. Image reconstruction and analysis

Images were reconstructed by filtered backprojection. A Lak kernel and a ramp filter apodized by a Hanning window with 8 lp/cm cutoff were employed to simulate both "bone"

and "soft tissue" reconstructions. Images of a 40×40 cm region were reconstructed with 0.5×0.5 mm pixels.

The various energy-weighting schemes result in different reconstructed CT numbers. For example, energy-integrating weighting, which more heavily weights the high energy photons, results in images with lower reconstructed CT numbers. In other words, the different weighting schemes result in images reconstructed at different effective energies. All reconstructed images were converted to Hounsfield units (HUs) using Eq. (21) which assumes an attenuation of water equal to 0.2 cm^{-1}. Based on this conversion, the reconstructed HU value of water varied depending on the energy-weighting scheme. To maintain the traditional definition of a Hounsfield unit (i.e., water equal to zero, all other intensities based on the fractional difference compared to water), the effective attenuation of water could be measured for each weighting scheme and used in Eq. (21). The CNR is unaffected by the conversion to Hounsfield units,

$$ \text{HU} = 1000 \cdot \frac{\mu - 0.2}{0.2}. \tag{21} $$

The optimal image-based and projection-based weighting schemes were compared with respect to CNR and beam-hardening artifacts. For both the breast and thorax applications, 25×25 pixel ROIs were extracted from the contrast element of interest and the background tissue. The background ROI was located at the same distance from isocenter as the contrast element ROIs. The mean and standard deviation of the HU values were determined in each ROI, and the CNR calculated with Eq. (22),

$$ \text{CNR} = \frac{\left| \text{HU}_{\text{signal}} - \text{HU}_{\text{background}} \right|}{\sigma_{\text{background}}}. \tag{22} $$

To quantify the beam-hardening cupping artifacts in the breast phantom images, reconstructions were performed from noise-free data with optimal weights derived from data with realistic noise. The percentage of cupping was quantified from the reconstructed values at the edge and center of the phantom, as described in Eq. (23),

$$ \% \, \text{cupping} = 100 \cdot \frac{\mu_{\text{edge}} - \mu_{\text{center}}}{\mu_{\text{edge}}}. \tag{23} $$

All simulations and reconstructions were repeated ten times to determine statistically significant differences between the investigated weight-calculation methods (A–D) and the energy-weighting schemes (optimal projection-based and image-based weighting).

III. RESULTS

All results pertain to images reconstructed with the apodized ramp filter unless otherwise indicated.

III.A. Optimal image-based weights

Figure 1 displays the unweighted breast phantom images reconstructed from each of the five energy bins. The noise standard deviation and the contrast between the background
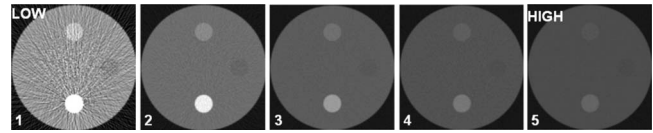
FIG. 1. Breast phantom images reconstructed from the five simulated detector energy bins. Level (HU): 750; width (HU): 2250.

breast tissue and the contrast elements are plotted in Fig. 2 for each energy bin. Similar trends were found in the thorax simulation. Photon-starvation effects were evident only in the lowest energy bin, with 0.7% of detector pixels measuring zero counts in the breast simulations, and 4% in the thorax simulations. The optimal image-based weights calculated by methods A–D are plotted in Fig. 3 for the breast simulations and in Fig. 4 for the thorax simulations.

III.B. Reconstructed images

Figure 5 compares breast-phantom images reconstructed with energy-integrating, photon-counting, optimal projection-based, and optimal image-based energy weighting. All images are displayed at the same window width of 2500 HU but with level corresponding to the HU value at the edge of the phantom. Figure 5 also plots the profiles through the CaCO$_3$ contrast element reconstructed by each energy-weighting scheme. Figure 6 displays thorax images reconstructed by each of the energy-weighting schemes along with profiles through the heart. Figure 7 displays images reconstructed with the Lak kernel.

III.C. CNR comparison

The CNR between the contrast elements and the background was calculated for each weight-calculation method and for all ten trials. A one-way repeated measure ANOVA analysis on the CNR of each contrast element indicated significant differences between the weighting methods ($p < 0.0005$). Subsequent paired T-tests did not find a significant difference in CNR between weights calculated by estimating noise in the image data (Methods A and C) and weights calculated by estimating noise in the projection data (Methods B and D). The task-specific weights (methods A and B) provided a small (1%–6%) but significant improve-
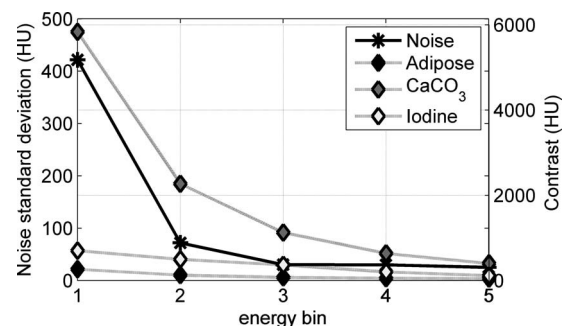

FIG. 2. Noise standard deviation and contrast between the phantom elements and the 50% glandular/50% adipose breast background for each energy-bin image.
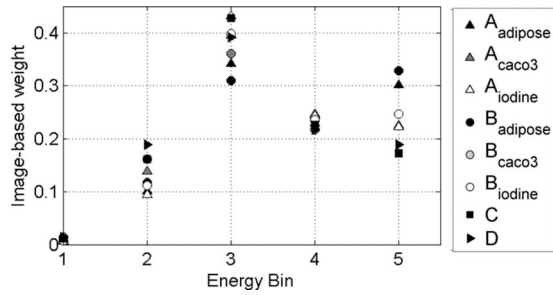
FIG. 3. Optimal image-based weights resulting from the eight weight-calculation methods investigated in the breast CT simulation. For example, the weights labeled $A_{adipose}$ correspond to the optimal weights calculated with method A for the specific task of optimizing the CNR between adipose and breast tissue.

FIG. 5. (left) Breast phantom images reconstructed with energy-integrating (EI), photon counting (PC), projection-based optimal weighting (PB), and image-based optimal weighting (IB). The optimal projection-based weights were optimized for the task of depicting $CaCO_3$ in breast tissue. Level (HU): EI=105; PC=180; PB=450; IB=185; width (HU): 2500. (right) Central vertical profile through the $CaCO_3$ element.

ment in CNR compared to the task-independent weights (methods C and D) ($p < 0.05$). Table IV summarizes the improvement in CNR obtained by using the task-specific image-based weights compared to the task-independent weights for each contrast element. Since the differences between weight-calculation methods A–D were small, all further image-based results were reconstructed with the weights of method D.

Table V summarizes the improvement in CNR compared to energy-integrating weighting. These results are in good agreement with a published study of optimal projection-based weighting whose results are also listed in Table V.[2] Images reconstructed with the Lak kernel resulted in similar CNR improvement factors (within 3% of the values in Table V).

The CNR values obtained by optimal image and projection-based weighting were compared with a two-sample T-test. Compared to optimal projection-based weighting, optimal image-based weighting provided a small but statistically significant 1.15 improvement in the CNR of the $CaCO_3$ element ($p < 0.005$). No significant difference was found between the optimal projection and image-based weighting for the adipose and iodine contrast elements.

III.D. Beam hardening comparison

The beam-hardening cupping metric [Eq. (23)] resulting from each energy-weighting scheme is listed in Table VI. To further depict the differences in beam-hardening artifact, the
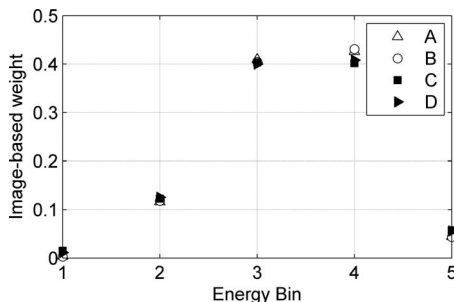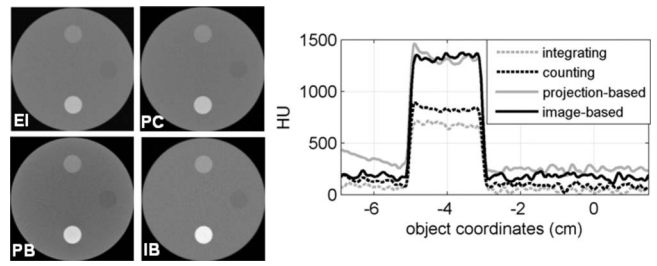
central horizontal profile through noise-free reconstructed breast phantom images is plotted in Fig. 8 for each energy-weighting scheme. To facilitate comparison, the profiles of reconstructed linear attenuation coefficients were normalized to have a value of 1 at the edge of the breast phantom. Figures 9 and 10 compare the beam-hardening artifacts in the spine and sternum regions of the throax phantom for optimal projection and image-based weighting.

IV. DISCUSSION AND CONCLUSIONS

The results of all experiments demonstrated that CT with optimally weighted energy-resolved data increased the CNR compared to energy-integrating and photon-counting detection. The results are in good agreement with a published study of optimal projection-based weighting whose results are also listed in Table V.[2] Unlike the detector simulated in the current study, the previous study simulated an energy-discriminating detector with realistic energy resolution.

The task-independent weights provided nearly the same CNR as the task-specific weights despite the limitations of the $1/E^3$ approximation. The benefits of using the task-specific weights were small ($\leq 6\%$ CNR improvement) with the most benefit for the adipose and iodine elements. Overall, the task-specific weights may be advantageous for low atomic number materials or materials with K-edges in the detected energy range. If task-specific weights are found to be beneficial for certain applications, image-based energy weighting has the additional advantage of easily varying the weights at the time of display and across the field of view.

FIG. 4. Optimal image-based weights resulting from the four weight-calculation methods investigated in the thorax simulation.
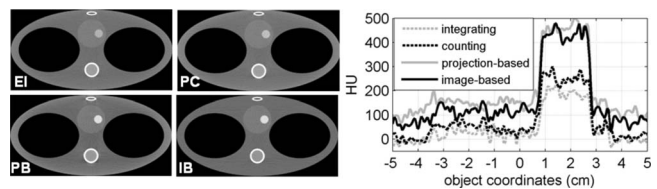

FIG. 6. (left) Thorax phantom images reconstructed with energy-integrating (EI), photon counting (PC), projection-based optimal weighting (PB), and image-based optimal weighting (IB). Level (HU): EI=20, PC=40, PB=150, IB=120. Width (HU): 800. (right) Central horizontal profile through the iodine element.
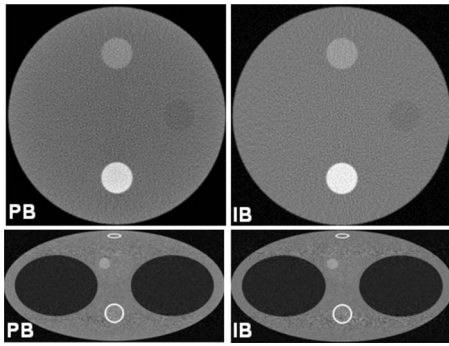
FIG. 7. Images reconstructed with the Lak kernel after projection-based optimal weighting (PB) and image-based optimal weighting (IB). Level (HU): $PB_{breast}=450$, $PB_{thorax}=150$, $IB_{breast}=185$, $IB_{thorax}=120$. Width (HU): 2500.

The optimal image-based weighting scheme produced negligible beam-hardening artifacts compared to all other energy-weighting schemes. Image-based weighting improved the CNR of $CaCO_3$ by a factor of 1.15 compared to optimal projection-based weighting, while no significant improvement was found for the CNR of adipose tissue and iodine. These CNR results may be explained by the fact that projection-based weights are optimized for maximizing the CNR in the projection data, but the contrast and noise transfer in a complex way through the logarithm. For example, consider the expressions for the optimal projection and image-based weights [Eqs. (2) and (8)]. The numerators in these expressions represent the contrast in the projection and reconstructed image, respectively. When the size and contrast of the embedded element are small, $\exp(-[\mu_c(E) - \mu_b(E)]d) \approx 1 - [\mu_c(E) - \mu_b(E)]d$ (Ref. 2) and the numerators of both expressions are equivalent to within the constant d. In other words, when the contrast is small, as is the case for the adipose and iodine elements in the breast simulation, the contrasts in the projection and image follow similar energy dependencies. When the contrast is large, as is the case for the calcium element, the contrasts in the projection and reconstructed image have different energy dependencies. Because the image-based weights take into account the energy dependencies in the reconstructed image, improved CNR may be possible.

Because the investigated reconstruction kernels were constant across energy bin, the choice of reconstruction kernel did not impact the relative CNR performance of the energy-weighting methods. Further image quality improvements may be possible by varying the kernel across the energy bins.

Future investigations of optimal image-based energy weighting must consider the constraints of a realistic detector, for example, studying the effects of imperfect energy resolution, detection efficiency, and limited count rates. The

effects of energy weighting on the scatter signal must also be investigated. Any reconstruction that more heavily weights low energy photons is expected to increase the effects of scatter.[12] Compared to optimal projection-based weighting, image-based weighting may incur an additional scatter penalty because scatter reduces the noise variance. The reduced noise variance will lead to increased weighting of bins that contain scatter. Additional simulation and experimental work is required to quantify this effect. An alternative approach for reconstructing images free of beam-hardening artifacts from energy-resolved data is to generate monoenergetic images using dual-energy methods. Future work must compare the dual-energy and optimal image-based weighting methods with respect to contrast and noise.

In summary, optimal image-based weighting of energy-resolved CT data improved the CNR by factors of 1.15–1.6 compared to energy-integrating weighting and factors of 1.0–1.3 compared to photon-counting weighting. Whereas optimal projection-based energy weighting increased beam-hardening effects, optimal image-based weighting provided comparable CNR with negligible beam-hardening artifacts.

ACKNOWLEDGMENTS

APPENDIX A: ALTERNATE METHOD OF PROJECTION-BASED ENERGY WEIGHTING

The projection-based weighting described in Eq. (3) weights and combines the energy-bin data before the raw-beam normalization and logarithm operations. For energy-resolving detectors, it is also possible to weight and combine the energy-bin data after normalization but before the logarithm. The resulting estimated line integral is

TABLE V. CNR improvement factor compared to energy-integrating weighting.

Weighting scheme	Adipose	CaCO$_3$	Iodine (breast)	Iodine (thorax)
Photon counting	1.11	1.16	1.16	1.25
Optimal image-based	1.15	1.50	1.31	1.57
Optimal projection-based	1.17	1.31	1.27	1.59
Optimal projection-based[2]	1.17	1.33	1.27	N/A

TABLE IV. Improvement in CNR obtained with task-specific weights compared to task-independent weights.

Adipose	CaCO$_3$	Iodine (breast)	Iodine (thorax)
1.06	1.01	1.04	1.02

TABLE VI. Percent beam-hardening cupping artifact [Eq. (23)].

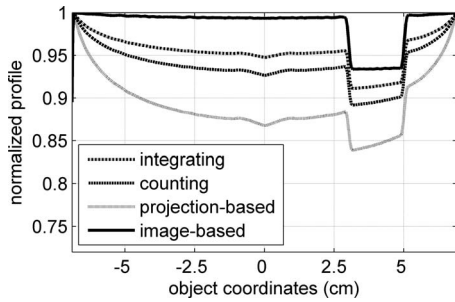| Energy integrating (%)	Photon counting (%)	Projection based (%)	Image based (%)
5.2	7.3	12.8	0.6

FIG. 8. Normalized central horizontal profiles through noise-free breast phantom images reconstructed with different energy-weighting schemes.

$$\widetilde{\ell}_{pb2} = -\ln\left(\sum_{i=1}^{M} w_i \cdot \frac{\int_{E_i} N_o(E) e^{-\int \mu(l,E)dl} dE}{\int_{E_i} N_o(E) dE}\right). \tag{A1}$$

In this case, the optimal weights must be proportional to the contrast-to-noise-variance ratio of the transmission ($T = N/N_o$). Consider two detector pixels: one detects N_b photons that travel through the background material and the other detects N_c photons that travel through the contrast element. The contrast in the transmission of these two beams, $C_{\text{transmission}}$, is equal to

$$C_{\text{transmission}} = \left| \frac{N_c}{N_o} - \frac{N_b}{N_o} \right|, \tag{A2}$$

where we assume that both beams have the same number of incident photons, N_o.

The noise variance of $C_{\text{transmission}}$ is equal to $\sigma^2_{\text{transmission}}$,

$$\sigma^2_{\text{transmission}} = \frac{\sigma^2_{N_c}}{N_o^2} + \frac{\sigma^2_{N_b}}{N_o^2} = \frac{N_c}{N_o^2} + \frac{N_b}{N_o^2}. \tag{A3}$$

The optimal weights for combining the transmission energy-bin data are proportional to the contrast-to-noise-variance ratio,

$$w(E) = \frac{|N_c(E) - N_b(E)|}{N_c(E) + N_b(E)} \cdot N_o(E). \tag{A4}$$

The weights in Eq. (A4) are equal to the weights of Eq. (2) multiplied by the number of incident photons at each energy.

Following the beam-hardening analysis of Sec. II A 3 and assuming monoenergetic energy bins and a homogeneous slab object of attenuation μ and thickness t, the line integral
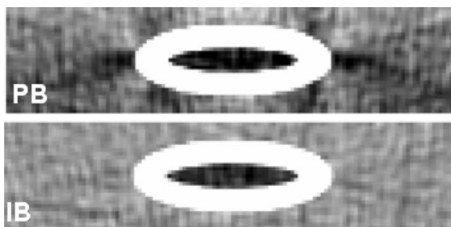

FIG. 9. Comparison of the sternum region in images reconstructed with optimal projection-based and image-based weights. Level (HU): PB=150, IB=75. Width (HU): 200.
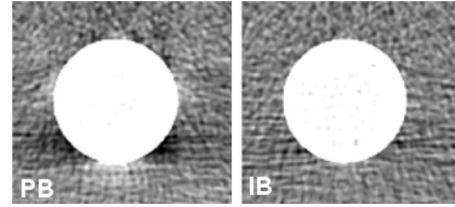
FIG. 10. Comparison of the spine region in images reconstructed with optimal projection-based and image-based weights. Level (HU): PB=120, IB =70. Width (HU): 200.

estimated by the alternate projection-based weighting scheme has a nonlinear dependence on t as shown in Eq. (A5), leading to beam-hardening artifacts,

$$\widetilde{\ell}_{pb2} = -\ln\left(\sum_{i=1}^{M} w_i \cdot e^{-\mu_i t}\right). \tag{A5}$$

The simulations described in Sec. II B were repeated with this alternate method of projection-based weighting. The resulting CNR and beam-hardening cupping values were within 5% of the original projection-based results.

An interesting relationship between projection-based and image-based weighting can be derived by comparing the estimated transmission values, which are obtained by exponentiating the negative of the estimated line integrals $\widetilde{\ell}_{pb2}$ [Eq. (A5)] for projection-based weighting and $\widetilde{\ell}_{ib}$ [Eq. (15)] for image-based weighting). As seen in Eqs. (A6) and (A7), the projection-based estimate of the transmission $\widetilde{T}_{pb2}$ is a weighted arithmetic mean of the energy-bin transmission data, while the image-based estimate, $\widetilde{T}_{ib}$, is a weighted geometric mean. The geometric mean is the more appropriate estimate of central tendency when the measurements represent ratios, as is the case of transmission measurements,[23]

$$\widetilde{T}_{pb2} = \sum_{i=1}^{M} w_i \cdot \frac{N_i}{N_o(E_i)}, \tag{A6}$$

$$\widetilde{T}_{ib} = \prod_{i=1}^{M} \left(\frac{N_i}{N_o(E_i)}\right)^{w_i}. \tag{A7}$$

a)Electronic mail: taly.gilat-schmidt@marquette.edu

[1] R. E. Alvarez and A. Macovski, "Energy-selective reconstructions in x-ray computerised tomography," Phys. Med. Biol. **21**(5), 733–744 (1976).

[2] P. M. Shikhaliev, "Computed tomography with energy-resolved detection: a feasibility study," Phys. Med. Biol. **53**(5), 1475–1495 (2008).

[3] P. M. Shikhaliev, "Energy-resolved computed tomography: first experimental results," Phys. Med. Biol. **53**(20), 5595–5613 (2008).

[4] R. E. Alvarez and E. Seppi, "A comparison of noise and dose in conventional and energy selective computed tomography," IEEE Trans. Nucl. Sci. **26**(8), 2853–2856 (1979).

[5] E. Roessl and R. Proksa, "K-edge imaging in x-ray computed tomography using multi-bin photon counting detectors," Phys. Med. Biol. **52**(15), 4679–4696 (2007).

[6] J. P. Schlomka, E. Roessl, R. Dorscheid, S. Dill, G. Martens, T. Istel, C. Bäumer, C. Herrmann, R. Steadman, G. Zeitler, A. Livne, and R. Proksa, "Experimental feasibility of multi-energy photon-counting K-edge imaging in pre-clinical computed tomography," Phys. Med. Biol. **53**(15), 4031–4047 (2008).

[7]M. J. Tapiovaara and R. F. Wagner, "SNR and DQE analysis of broad spectrum x-ray imaging," Phys. Med. Biol. **30**(6), 519–529 (1985).

[8]P. M. Shikhaliev, "Tilted angle CZT detector for photon counting/energy weighting x-ray and CT imaging," Phys. Med. Biol. **51**(17), 4267–4287 (2006).

[9]P. M. Shikhaliev, "Beam hardening artefacts in computed tomography with photon counting, charge integrating and energy weighting detectors: a simulation study," Phys. Med. Biol. **50**(24), 5813–5827 (2005).

[10]J. Giersch, D. Niederlohner, and G. Anton, "The influence of energy weighting on x-ray imaging quality," Nucl. Instrum. Methods Phys. Res. A **531**(1–2), 68–74 (2004).

[11]S. S. Gleason, H. Sari-Sarraf, M. J. Paulus, D. K. Johnson, S. J. Norton, and M. A. Abidi, "Reconstruction of multi-energy x-ray computed tomography images of laboratory mice," IEEE Trans. Nucl. Sci. **46**, 1081–1086 (1999).

[12]D. Niederlohner, J. Karg, J. Giersch, M. Firsching, and G. Anton, "Practical aspects of energy weighting in x-ray imaging," *IEEE Nuclear Science Symposium Conference Record, 2004* (unpublished), Vol. 5, pp. 3191–3194.

[13]D. Niederlohner, F. Nachtrab, T. Michel, and G. Anton, "Using the Medipix2 detector for photon counting computed tomography," *IEEE Nuclear Science Symposium Conference Record, 2005* (unpublished), Vol. 4, pp. 2327–2331.

[14]E. V. de Casteele, D. V. Dyck, J. Sijbers, and E. Raman, "An energy-based beam hardening model in tomography," Phys. Med. Biol. **47**(23), 4181–4190 (2002).

[15]J. M. Boone and J. A. Seibert, "An accurate method for computer-generating tungsten anode x-ray spectra from 30 to 140 kV," Med. Phys. **24**(11), 1661–1670 (1997).

[16]J. M. Boone, A. Kwan, J. Seibert, N. Shah, K. Lindfors, and T. Nelson, "Technique factors and their relationship to radiation dose in pendant geometry breast CT," Med. Phys. **32**(12), 3767–3776 (2005).

[17]J. A. Seibert, "X-ray imaging physics for nuclear medicine technologists. Part 1: Basic principles of x-ray production," J. Nucl. Med. Technol. **32**(3), 139–147 (2004).

[18]"FORBILD Thorax phantom." http://www.imp.uni-erlangen.de/forbild/english/forbild/index.htm.

[19]"Tissue substitutes in radiation dosimetry and measurement," ICRU, Technical Report No. 44, 1989.

[20]"NIST: Tables of x-ray mass attenuation coefficients and mass energy-absorption coefficients," National Institute of Standards and Technology, Gaithersburg http://physics.nist.gov/PhysRefData/XrayMassCoef/cover.html.

[21]P. M. Shikhaliev, T. Xu, and S. Molloi, "Photon counting computed tomography: concept and initial results," Med. Phys. **32**(2), 427–436 (2005).

[22]D. A. Chesler, S. J. Riederer, and N. J. Pelc, "Noise due to photon counting statistics in computed x-ray tomography," J. Comput. Assist. Tomogr. **1**(1), 64–74 (1977).

[23]H. F. Weisberg, *Central Tendency and Variability*, 3rd ed. (Sage, Newbury Park, CA, 1992), pp. 41–43.